Information content of the weak-charge form factor

Reinhard, P.-G.; Piekarewicz, J.; Nazarewicz, W.; Agrawal, B. K.; Paar, Nils; Roca-Maza, X.

Information content of the weak-charge form factor

P.-G. Reinhard,[1] J. Piekarewicz,[2] W. Nazarewicz,[3,4,5] B. K. Agrawal,[6] N. Paar,[7] and X. Roca-Maza[8]
[1]*Institut für Theoretische Physik II, Universität Erlangen-Nürnberg, Staudtstrasse 7, D-91058 Erlangen, Germany*
[2]*Department of Physics, Florida State University, Tallahassee, Florida 32306, USA*
[3]*Department of Physics & Astronomy, University of Tennessee, Knoxville, Tennessee 37996, USA*
[4]*Physics Division, Oak Ridge National Laboratory, Oak Ridge, Tennessee 37831, USA*
[5]*Faculty of Physics, University of Warsaw, ul. Hoża 69, 00-681 Warsaw, Poland*
[6]*Saha Institute of Nuclear Physics, Kolkata 700064, India*
[7]*Physics Department, Faculty of Science, University of Zagreb, Zagreb, Croatia*
[8]*Dipartimento di Fisica, Università degli Studi di Milano and INFN, 20133 Milano, Italy*
(Received 7 August 2013; published 30 September 2013)

Background: Parity-violating electron scattering provides a model-independent determination of the nuclear weak-charge form factor that has widespread implications across such diverse areas as fundamental symmetries, nuclear structure, heavy-ion collisions, and neutron-star structure.
Purpose: We assess the impact of precise measurements of the weak-charge form factor of ^{48}Ca and ^{208}Pb on a variety of nuclear observables, such as the neutron skin and the electric-dipole polarizability.
Methods: We use the nuclear density functional theory with several accurately calibrated nonrelativistic and relativistic energy density functionals. To assess the degree of correlation between nuclear observables and to explore systematic and statistical uncertainties on theoretical predictions, we employ the chi-square statistical covariance technique.
Results: We find a strong correlation between the weak-charge form factor and the neutron radius, that allows for an accurate determination of the neutron skin of neutron-rich nuclei. We determine the optimal range of the momentum transfer q that maximizes the information content of the measured weak-charge form factor and quantify the uncertainties associated with the strange quark contribution. Moreover, we confirm the role of the electric-dipole polarizability as a strong isovector indicator.
Conclusions: Accurate measurements of the weak-charge form factor of ^{48}Ca and ^{208}Pb will have a profound impact on many aspects of nuclear theory and hadronic measurements of neutron skins of exotic nuclei at radioactive-beam facilities.

DOI: 10.1103/PhysRevC.88.034325 PACS number(s): 21.10.Gv, 21.60.Jz, 21.65.Mn, 25.30.Bf

I. INTRODUCTION

The lead radius experiment ("PREX") at the Jefferson Laboratory has used parity-violating electron scattering to probe the weak-charge density distribution in ^{208}Pb [1,2]. Given that the weak charge of the neutron is much larger than that of the proton, parity-violating electron scattering provides a clean probe of neutron densities [3]. The parity-violating asymmetry calculated within the Born approximation, although qualitative, is directly proportional to the weak-charge form factor, which in turn is obtained from the weak-charge density by a Fourier transform. This direct relation is preserved in calculations that account for Coulomb distortions [4,5]. PREX measured the weak-charge form factor of ^{208}Pb at a momentum transfer of $q_{\rm PREX} = 0.475\,{\rm fm}^{-1}$ to be [2]

$$F_W(q_{\rm PREX}) = 0.204 \pm 0.028. \tag{1}$$

By making some assumptions pertaining to the form factor, PREX was able to provide the first determination of the neutron-skin of ^{208}Pb [1]:

$$r_{\rm skin}^{208} = r_n^{208} - r_p^{208} = 0.33^{+0.16}_{-0.18}\ {\rm fm}, \tag{2}$$

where r_n^{208} (r_p^{208}) is the neutron (proton) root-mean-square (rms) radius of ^{208}Pb. Although PREX demonstrated excellent control of systematic errors, the statistical accuracy of the measurement was compromised. Fortunately, the PREX Collaboration has made a successful proposal ("PREX-II") [6] that will allow them to reach their original goal of 0.06 fm in the experimental uncertainty.

Given that PREX demonstrated that model-independent measurements of the weak-charge form factor in heavy nuclei are now feasible, it is pertinent to ask whether a measurement in a different neutron-rich nucleus could prove advantageous. Indeed, the case of ^{48}Ca seems particularly attractive for several reasons. First, ^{48}Ca is a doubly-magic nucleus that is already within the reach of *ab initio* calculations [7,8]. Thus, the recently approved calcium radius experiment ("CREX") [9] could provide a critical bridge between *ab initio* approaches and density functional theory. Second, by providing this kind of bridge, CREX will help elucidate the character of the three-nucleon force, or the density dependence of the energy density functional, which play a critical role in determining the limits of the nuclear landscape [10–13] and properties of nuclear and neutron matter [14–16]. Finally, CREX—together with PREX-II—will provide calibrated benchmarks for hadronic measurements of neutron skins at radioactive beam facilities. Note that the CREX collaboration has made a successful proposal to measure the neutron radius of ^{48}Ca using parity-violating electron scattering with an unprecedented accuracy of 0.02 fm [9]. This has a great potential to guide further theoretical developments [17,18].

Among the great variety of nuclear structure models, self-consistent mean-field (SCMF) models rooted in the nuclear density functional theory (DFT) provide the best compromise between accuracy, computational expediency, and universality (by covering the greatest range of accessible nuclei) [19,20]. This survey is concerned with the performance of SCMF models in relation to the weak-charge form factor and its possible impact on improving energy density functionals (EDFs) that are at the heart of the SCMF approaches.

The structure of all EDFs can be motivated on formal grounds by invoking methods such as density-matrix expansion that may be tested against *ab initio* approaches. Although enormous progress has been made in developing *ab initio* techniques, at present they are of limited use in building the spectroscopic quality of EDFs. Thus, the coupling constants of EDFs, i.e., model parameters, must be determined empirically through a fit to selected nuclear data. Once determined, often through the minimization of an appropriate objective function, the parameters are universal in that the same functional can in principle be applied to all nuclei, nuclear reactions, and neutron stars.

Such an empirical fit also provides valuable information on the statistical uncertainties of the model parameters and the correlations between them. This is of particular importance in the context of the isovector sector of the EDFs. Indeed, whereas the isoscalar sector of the density functional is fairly well determined by the pool of available nuclear data (such as ground-state masses and charge radii), the isovector sector is hindered by the sparsity of high-quality data that are sensitive to the neutron-proton asymmetry. This implies that all isovector-sensitive observables, such as the neutron skin and electric-dipole polarizability of neutron-rich nuclei, are predicted with large theoretical uncertainties. However, those uncertainties can be turned into an advantage by allowing us to explore correlations between different observables. Indeed, it was through such a statistical covariance analysis that a strong correlation between the electric dipole polarizability and the neutron skin of ^{208}Pb was established [21]. We wish to emphasize that theoretical uncertainties and correlations among observables are estimated within a given model by computing the covariance matrix associated with the minimization of the associated objective function [18,21–25]. Although such an approach provides the statistical uncertainties and correlations, it cannot assess the systematic errors that reflect constraints and limitations of a given model. Such systematic uncertainties can only emerge by comparing different models [17,18,26]. It is the aim of the present paper to apply both statistical and systematic (or trend) analyzes to investigate uncertainties and correlations associated to the weak-charge form factor at the momentum transfers of relevance to PREX-II and CREX.

The manuscript has been organized as follows. In Sec. II we develop the formalism required to carry out the correlation analysis for a variety of accurately-calibrated SCMF models. Results are presented in Sec. III for the correlations between various observables using both a trend and a covariance analysis. We summarize our results and present the outlook for the future in Sec. IV.

II. FORMALISM

In this section we introduce the SCMF models used in the present survey, the observables discussed, and the details of the statistical covariance analysis.

A. SCMF models

In this survey we compare results from two different nuclear EDFs: the nonrelativistic Skyrme-Hartree-Fock (SHF) and the relativistic mean-field (RMF) models. There is some variety among the relativistic models. Here we will consider the standard nonlinear (NL) RMF, its point-coupling (PC) variant, its extension from Florida State University (FSU), and finally the relativistic model with density dependent meson-nucleon couplings (DDME). We now briefly summarize the essential features and fitting protocols of the various functionals.

1. Nonrelativistic Skyrme-Hartree-Fock (SHF) model

The SHF model uses an EDF which is constructed from baryon, spin-orbit, and kinetic-energy densities. Each interaction term (including the spin-orbit term) appears in isoscalar and isovector form. This provides the model with great flexibility in the isovector channel. Note that SHF has, unlike the RMF model, explicit independent parameters for the spin-orbit coupling. The functional has altogether about ten free parameters. Pairing is modeled by a density-dependent contact interaction having three further free parameters. For details see [19,22,23]. Here, we shall use the SV parametrizations from Ref. [22]. These fits were done to a large pool of semimagic nuclei that were checked to have negligible correlation effects [27]. The observables included in the SV optimization database are binding energy (70 entries), rms charge radius (50 entries), charge diffraction radius (28 entries), charge surface thickness (26 entries), neutron and proton pairing gaps (37 entries), and spin-orbit splittings of single-particle energies (7 entries). An objective function χ^2 was calibrated to these data and its minimization yields the SV-min parametrization that will be used here for the correlation analysis (see below). We have also provided a couple of further parametrizations with systematic variation of nuclear matter properties (incompressibility K, isoscalar effective mass m^*/m, symmetry energy at the saturation density J, and TRK sum rule enhancement κ related to isovector effective mass). To this end, these four properties are constrained in a fit using the same data as for SV-min. Several fits of that sort are run producing four chains each one varying exclusively one of these nuclear matter properties. This set of parametrizations is used for the trend analysis.

2. Traditional relativistic mean-field model (RMF)

The RMF model consists of Dirac nucleons interacting via the exchange of three *mesons*: an isoscalar-scalar σ meson, an isoscalar-vector ω meson, and an isovector-vector ρ meson. The corresponding baryon densities become the sources for the meson-field equations that are solved at the mean-field level. In turn, the meson fields provide the scalar and vector potentials that enter into the Dirac equation. This procedure is repeated until self-consistency is achieved [28].

A quantitatively successful RMF model emerges when these three Yukawa couplings were augmented by a nonlinear (NL) self-coupling of the σ meson [29]. This had led to some successful applications throughout the nuclear chart, first NL1 [30] and then NL3 [31]; for some reviews see Refs. [32,33]. However, with increasing demands on quality predictions, several deficiencies of the original nonlinear models became apparent. For example, both the incompressibility of symmetric nuclear matter and the slope of the symmetry energy were notoriously high as compared to SHF models. In particular, this hindered the description of giant monopole resonances (GMRs) over a larger mass range [34]. In particular, NL3 overestimates the location of the breathing mode in ^{90}Zr—a nucleus with a well developed GMR peak but small neutron-proton asymmetry.

3. FSU RMF model

In response to these shortcomings, a new FSUGold parametrization was developed [35] by extending the NL3 model by two additional terms in order to soften both the equation of state of symmetric nuclear matter and the symmetry energy. Following standard practices, FSUGold was accurately calibrated through the minimization of χ^2 constrained by the binding energies and charge radii of magic nuclei, as well as some bulk properties of nuclear matter. The slight extension of the model allowed FSUGold to generate a smaller incompressibility coefficient and a softer symmetry energy, which proved essential in reproducing simultaneously the GMR in both ^{90}Zr and ^{208}Pb, as well as the isovector giant dipole resonance in ^{208}Pb. We note, however, that at the time of the calibration of the FSUGold interaction, no covariance matrix was extracted. Hence, the correlation coefficients predicted in the present work by FSUGold (or "FSU" for short) are obtained from the simplified covariance analysis presented in Ref. [24]. As in the nonrelativistic case, trends will also be studied by producing NL and FSU chains (or "families") through a systematic variation of the model parameters. In the case of NL and FSU, the systematic variations are implemented by only varying the two isovector parameters of the model; the isoscalar sector remains intact. For details on the implementation we refer the reader to Refs. [36,37].

4. Density dependent RMF model

We also employ two other variants of the RMF model. The RMF-DDME functional is based on the standard form of Yukawa-coupled nucleon-meson interactions, but with the coupling constants supplemented with an elaborate density dependence [38]. Modeling the density dependence introduces four additional free parameters which brings to 8 the total number of parameters in RMF-DDME. In the RMF-PC model one effectively eliminates the mesons by making their masses much larger than any scale in the problem. In this model, nucleons interact via four-fermion contact interactions or equivalently, via point coupling terms that are quadratic in the various baryon densities [39]. Similar to the NL models, nonlinearities are introduced through cubic and quartic terms in the scalar density. Finally, to compensate for the finite range of the (missing) meson fields, the model is supplemented with derivative (or gradient) coupling terms involving the two vector densities. This amounts to 9 free parameters for the RMF-PC model. Both in DDME and PC variants of the RMF model, the pairing force is introduced by using the BCS approximation with empirical pairing gaps. Finally, in both cases, optimal parametrizations were obtained by fitting to the data set that includes ground-state binding energies, charge radii, diffraction radii, and surface thicknesses of 17 spherical nuclei ranging from ^{16}O to ^{214}Pb.

B. Nuclear observables

As we have seen above, basic ground-state observables, such as binding energies and charge radii are critical inputs for the calibration of the functional. Here we consider additional observables that were not included in the calibration and whose correlations we wish to explore. These are

(i) the root-mean-square neutron radius r_n;
(ii) the neutron skin $r_{\rm skin}$;
(iii) the weak-charge form factor $F_W(q)$;
(iv) the electric dipole polarizability α_D.

The rms radii are computed from the r^2 weighted density distribution. The weak-charge form factor $F_W(q)$ is obtained from the Fourier transform of the corresponding weak-charge density with the calibration $F_W(0) = 1$ (for details see Appendix). Finally, the electric dipole polarizability is computed in a random-phase approximation (RPA) from the inverse-energy weighted dipole strength $\alpha_D = 2\sum_n(|\langle\Phi_n|\hat{D}|\Phi_0\rangle|^2/E_n)$, where n runs over all excited states of the system. We note that the RPA is the consistent linear response of the mean-field ground state to external perturbations. We will compute these observables with a variety of EDFs for ^{48}Ca and ^{208}Pb in an effort to emphasize the importance of CREX and PREX-II. Besides these observables in finite nuclei, we will consider key response properties of symmetric nuclear matter: the incompressibility K, the symmetry energy J, and the density dependence of the symmetry energy L.

C. Correlating observables

1. Optimization by χ^2 minimization

Each EDF is characterized by about a dozen free parameters $\mathbf{p} = (p_1, \ldots, p_F)$ that are calibrated to a host of observables from finite nuclei. The most efficient and systematic implementation of the calibration procedure is through a least-squares fit. The fitting procedure starts with the definition of an objective function (quality measure) $\chi^2(\mathbf{p})$ that is computed by accumulating the squared residuals of calculated observables relative to the experimental data

$$\chi^2 = \sum_{i=1}^{N}\left[\frac{\mathcal{O}_i^{\rm exp.} - \mathcal{O}_i^{\rm theo.}(\mathbf{p})}{\sigma_i}\right]^2, \qquad (3)$$

and weighted by the corresponding one standard deviation σ_i associated with the ith observable. The optimum

parametrization $\mathbf{p}_0$ is the one that minimizes χ^2 with the minimum value given by $\chi^2_0 \equiv \chi^2(\mathbf{p}_0)$.

2. The space of reasonable model parameters

Model parameters $\mathbf{p}$ which lie in the immediate vicinity of $\mathbf{p}_0$ also provide a good description of the experimental data. Moreover, the trends in this vicinity encode a wealth of useful information which we can exploit in a covariance analysis. Specifically, the range of "reasonable" parametrizations is defined to cover all model parameters $\mathbf{p}$ for which $\chi^2(\mathbf{p}) \leqslant \chi^2_0 + 1$ [40]. Given that such a range of parameters is usually rather small, we can expand χ^2 in a power series around $\mathbf{p}_0$. That is, up to second order in $(\mathbf{p} - \mathbf{p}_0)$ we obtain

$$\chi^2(\mathbf{p}) - \chi^2_0 \approx \sum_{i,j=1}^{F} (\mathbf{p} - \mathbf{p}_0)_i \, \mathcal{M}_{ij} (\mathbf{p} - \mathbf{p}_0)_j \,, \tag{4}$$

where $\mathcal{M}_{ij}$ is the matrix of second derivatives:

$$\mathcal{M}_{ij} = \tfrac{1}{2} \partial_{p_i} \partial_{p_j} \chi^2(\mathbf{p})\big|_{\mathbf{p}_0}. \tag{5}$$

The reasonable parametrizations thus fill the confidence ellipsoid given by (see Sec. 9.8 of [40])

$$(\mathbf{p} - \mathbf{p}_0)^T \hat{\mathcal{M}} (\mathbf{p} - \mathbf{p}_0) \leqslant 1. \tag{6}$$

3. Correlations between observables

It is now interesting to examine the impact of the formulation on physical observables. Each set of model parameters $\mathbf{p}$ determines the functional, and thus any observable A predicted by such functional may be considered a function of the parameters, i.e., $A = A(\mathbf{p})$. For a Gaussian distribution $\exp[-\chi^2(\mathbf{p})]$ of the different parametrizations $\mathbf{p}$ around the minimum $\mathbf{p}_0$, the central value of the observable is given by $A_0 \equiv A(\mathbf{p_0})$ and there is an uncertainty in the value of A as one varies the $\mathbf{p}$ within the confidence ellipsoid. We now assume for simplicity that the observable varies slowly with $\mathbf{p}$ within the relevant range, so that we can estimate its uncertainty through a linear estimate. That is,

$$A(\mathbf{p}) \approx A_0 + (\mathbf{p} - \mathbf{p}_0) \cdot \partial_{\mathbf{p}} A|_{\mathbf{p}_0}. \tag{7}$$

The Gaussian-weighted average over the parameter landscape yields the combined uncertainties of two observables A and B, i.e., their covariance:

$$\overline{\Delta A \, \Delta B} = \sum_{ij} \big(\partial_{p_i} A\big)\big(\hat{\mathcal{M}}^{-1}\big)_{ij}\big(\partial_{p_j} B\big). \tag{8}$$

In the case of $A = B$, then Eq. (8) gives the variance $\overline{(\Delta A)^2}$, which defines the uncertainty of A. Variance and covariance are useful concepts that allow to estimate the impact of an observable on the model and its fit. We will exploit this in two ways by means of (i) a trend analysis and (ii) a covariance analysis. In the trend analysis, parameters of the optimum model are modified according to a change in a given bulk parameter of infinite nuclear matter and then the response of the observable of interest is monitored. For example, one could fix the slope of the symmetry energy L, then constrain the remaining model parameters to reproduce this value, and finally monitor how the neutron skin of ^{208}Pb responds to this change. Such a strategy helps elucidate systematic differences among the predictions of the models. In the covariance (or correlation) analysis, on the other hand, only information from the properly extracted covariance matrix $\hat{\mathcal{M}}^{-1}$ is used to compute statistical correlations within a given optimum model. A useful dimensionless statistical measure of correlation between two observables is the Pearson product-moment correlation coefficient [40]:

$$c_{AB} = \frac{|\overline{\Delta A \, \Delta B}|}{\sqrt{\overline{\Delta A^2}\;\overline{\Delta B^2}}}. \tag{9}$$

In particular, a value $c_{AB} = 1$ means that the two observables are fully correlated whereas a value of $c_{AB} = 0$ means that they are uncorrelated. Note that we do not distinguish between perfect correlation $c_{AB} = +1$ and perfect anticorrelation $c_{AB} = -1$.

III. RESULTS

In this section we present results for the correlations between observables. We start with the conceptually simpler trend analysis and continue with the more quantitative covariance analysis.

A. Trend analysis

A simple way to visualize the mutual dependence between isovector observables is to produce sets of parametrizations with systematically varied symmetry energy J and to study the behavior of a pair of observables along those sets (see, e.g., Refs. [22,26]). In the following, we compare the predictions of four different families of models (SHF, DDME, NL3, FSU) that cover a systematic variation of J. As displayed in Fig. 1, such a variation is reflected in systematic changes to strong isovector indicators, such as $r^{208}_{\rm skin} \equiv r_{\rm skin}[^{208}{\rm Pb}]$ and the associated weak-charge form factor $F^{208}_W \equiv F_W(q_{\rm PREX})[^{208}{\rm Pb}]$. Very strong correlations appear for *all* pairs of observables and for *all* model families.

As alluded earlier, F^{208}_W is strongly sensitive to the density dependence of the symmetry energy and this is reflected in its strong correlation with $r^{208}_{\rm skin}$, as displayed in Fig. 1(e). This strong correlation appears universal as *all models* lie practically on one line, suggesting that the experimentally extracted weak-charge from factor F^{208}_W from the parity-violating asymmetry provides a strong constraint on $r^{208}_{\rm skin}$ [1,2,5,42]. However, we observe a weaker intermodel correlation between these two observables and the electric dipole polarizability $\alpha_D[^{208}{\rm Pb}]$, see panels (a) and (b), and the weak-charge form factor of ^{48}Ca (F^{48}_W) in Figs. 1(c) and 1(d). The correlation between α^{208}_D and $r^{208}_{\rm skin}$ has been studied in Ref. [17] that has confirmed α^{208}_D as a key isovector indicator (see also discussion in Refs. [43,44]). We note that the electric dipole polarizability in ^{208}Pb was recently measured at the Research Center for Nuclear Physics (RCNP) using polarized proton inelastic scattering at forward angles. The reported value from such a landmark experiment is [41]

$$e^2 \alpha^{208}_D = (20.1 \pm 0.6)\ {\rm fm}^3 \,. \tag{10}$$

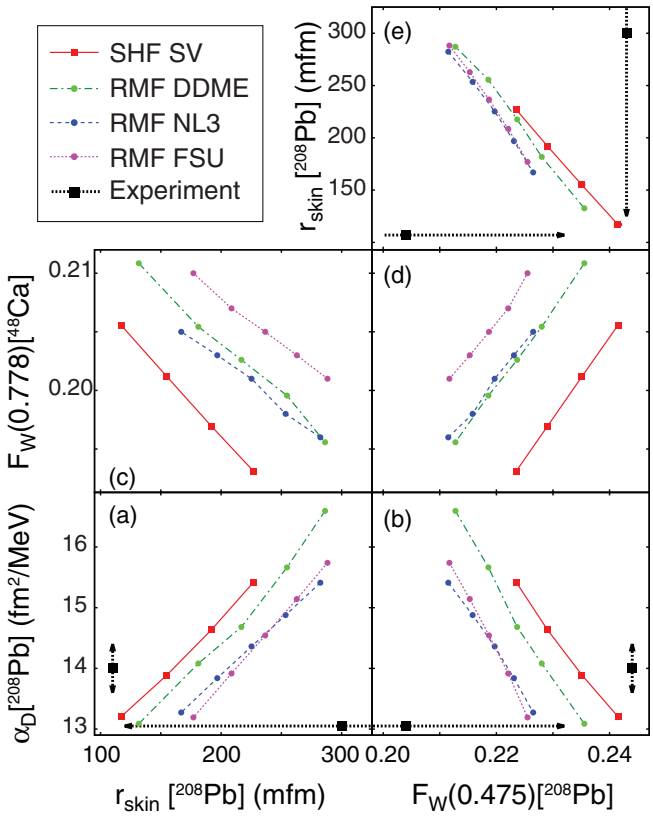

FIG. 1. (Color online) Systematic trends as predicted by the various families of models for the following isovector observables: the neutron skin, electric-dipole polarizability, weak-charge form factor $F_W(q = 0.475\ \text{fm}^{-1})$ of ^{208}Pb, and the weak-charge form factor $F_W(q = 0.778\ \text{fm}^{-1})$ of ^{48}Ca. Experimental values are indicated by black squares with error bars (r_{skin}^{208} and F_W^{208} from Refs. [1,2] and α_D^{208} from Ref. [41]).

Note that there two conventions for the units of the polarizability are commonly used. Some references [17,41], augment it with the charge factor $e^2 = 1.44$ MeV fm, thus expressing α_D in units of fm^3. Others, e.g., [21] and this work, use the dipole operator without charge, which leads to units fm^2/MeV.

In this work, we look for the first time into the correlation between the weak-charge form factors of ^{48}Ca and ^{208}Pb displayed in Fig. 1(d). In particular, we note a significant model variance of the correlation between F_W^{208} and F_W^{48}, suggesting that PREX-II and CREX provide complimentary information. Indeed, whereas PREX-II places powerful constrains on bulk nuclear-matter properties (primarily L), ^{48}Ca—with a significant larger surface-to-volume ratio than ^{208}Pb—may help constrain better surface properties of nuclear structure models by providing a powerful bridge between *ab initio* calculations and density functional theory.

In further comparing models in Fig. 1, we observe that the linear behavior displayed in the figure is characterized by nearly equal slopes for all models but different intercepts. It is interesting to note that there is a significant spread even among the RMF variants. Recall that DDME introduces density dependence directly into the meson-nucleon couplings whereas both NL3 and FSU incorporate density-dependent effects through nonlinear meson self-interactions and mixed terms. In particular, we note that models that predict the same r_{skin}^{208} show large variations in F_W^{48}, suggesting that a measurement of the neutron radius of ^{208}Pb is unable to constrain the neutron radius in ^{48}Ca [17]. This is likely to suggest significant differences in the surface properties of the models used. Preliminary explorations along these lines are now in progress.

Before leaving this section, we briefly summarize the main findings from trend analysis between F_W^{208}, F_W^{48}, r_{skin}^{208}, and α_D^{208}: All these observables are mutually related showing clear trends whose slope is the same for all models while the offset can differ significantly. Unambiguous is the correlation between F_W^{208} and r_{skin}^{208}. For the other pairs of observables, we see offsets. These point towards underlying differences in the models as density dependence and surface properties.

B. Covariance analysis

Having estimated the systematic uncertainties generated by various models, we now proceed to implement the correlation analysis directly in terms of the covariance matrix. To this end, we compute correlation coefficients (9) for all the models considered, directly in terms of their own covariance matrix (5). Figure 2(a) displays correlation coefficients between F_W^{208} and a suitable selection of physical observables and bulk parameters of infinite nuclear matter. The analogous information on F_W^{48} is shown in Fig. 2(b). The accurately calibrated models included in this comparison are SV-min (a SHF model) and three RMF variants: DDME-min1, PC-min1, and FSUGold. The first (topmost) entry illustrates the excellent correlation between F_W^{208} and F_W^{48} within each model. This is reminiscent of the strong correlation—within each model family—observed in Fig. 1(d). However, recall that as, systematic uncertainties across the various models are assessed, the correlation weakens significantly. These findings reinforce the argument in favor of combined measurements of F_W^{208} and F_W^{48}. Indeed, both PREX-II and CREX will provide invaluable information in discriminating among various SCMF models.

The second entry confirms the strong correlation between r_n^{208} and F_W^{208}. This suggest that although $q_{\text{PREX}} r_n^{208} \gtrsim 1$, thereby invalidating a direct extraction of r_n^{208} from F_W^{208}, measuring the form factor provides a strong constraint on the neutron radius [42]. The same strong correlations were found between r_n^{48} and F_W^{48} (not shown here) which thus allows the same conclusions for ^{48}Ca. Still, we stress that the cleanest comparison between theory and experiment is directly in terms of the experimentally measured form factor. We will look into this connection in more detail in Sec. III C.

The correlations with r_{skin} may seem surprising at first glance. There is an apparent dichotomy between SV-min and DDME-min1 on the one hand, and PC-min1 and FSUGold on the other. Whereas the former display a strong correlation between r_{skin}^{208} and F_W^{208}, the correlation weakens significantly for the latter. The apparent contradiction may have its origin in the underlying fitting protocols and different density dependence. For example, both SV-min and DDME-min1 include the charge radius of ^{208}Pb (r_{ch}^{208}) with its very small experimental

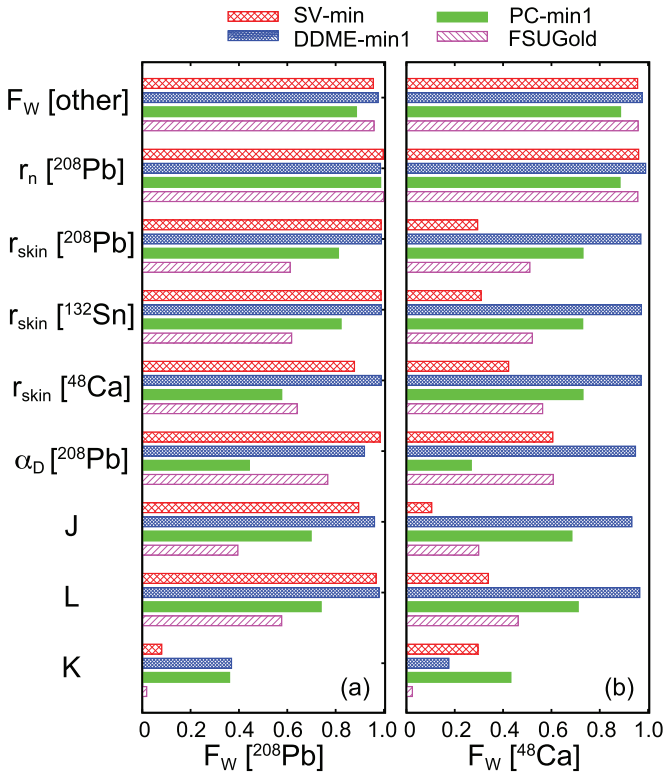

FIG. 2. (Color online) Correlation coefficients (9) derived from a covariance analysis between the weak-charge form factors of ^{208}Pb (F_W^{208}) and ^{48}Ca (F_W^{48}), and a variety of nuclear observables, including the strong isovector indicators such as neutron skin, electric dipole polarizability, symmetry energy J, slope of the symmetry energy L, and a strong isoscalar indicator: incompressibility K at saturation density. In all cases correlation coefficients are obtained from the covariance matrix associated with each model.

error [45] in the fit. Such a small error strongly constrains the linear combination of model parameters sensitive to the charge radius. This implies that the exploration of the model landscape is "locked" at the experimental value of $r_{\rm ch}^{208}$ (or equivalently r_p^{208}). Thus, any changes in $r_{\rm skin}^{208}$ around the optimal model are essentially generated by the corresponding changes in r_n^{208}. The charge radius of ^{208}Pb was also included in the calibration procedure of the FSUGold functional [35]. However, in contrast to SV-min and DDME-min1, no covariance matrix was extracted at that time. Thus, the FSUGold correlation coefficients presented in this work were obtained from a simplified covariance analysis of Ref. [24] that did not include $r_{\rm ch}^{208}$ into the fit. Clearly, as we develop next-generation EDFs, their optimization procedure should always generate both the optimal model as well as the covariance matrix. We note that, in the case of the correlation between F_W^{48} and $r_{\rm skin}^{48}$, DDME-min1 remains the sole model displaying a strong correlation; in the case of SV-min, the correlation is much weaker. Again, this difference may originate from the various fitting protocols.

In Ref. [21] the electric dipole polarizability in ^{208}Pb was identified as a strong isovector indicator that is strongly correlated to $r_{\rm skin}^{208}$. Here too we find a strong correlation between F_W^{208} and α_D^{208}, except for PC-min1 where this correlation appears to be fairly weak. Moreover, we note that the correlation between α_D^{208} and the weak-charge form factor of ^{48}Ca weakens significantly, with the exception of DDME-min1. Within the next few years we expect that CREX and PREX-II will provide accurate measurements of the neutron radius of ^{48}Ca and ^{208}Pb with anticipated errors of 0.02 fm and 0.06 fm, respectively. We note that a high-precision measurement of α_D^{208} is now available [41] and that the corresponding measurement on ^{48}Ca is presently being analyzed [46]. When combined, these four key isovector indicators will provide the critical input for the calibration of EDFs of increasing sophistication.

Finally, correlations between F_W^{208} and bulk parameters of infinite nuclear matter display a large model dependence. For example, both SV-min and DDME-min1 display a strong correlation between F_W^{208} and the symmetry energy J and the slope of the symmetry energy L at saturation density. This appears not to be the case for PC-min1 and FSUGold. As mentioned earlier, this reflects the simplified covariance analysis with FSUGold that failed to include a tightly constrained charge radius of ^{208}Pb into the fit. Finally, as an illustration, we show how a strong isoscalar indicator such as the incompressibility of symmetric nuclear matter K is weakly correlated with both weak-charge form factors in all the models.

C. Momentum-transfer sensitivity of the weak-charge form factor

So far we have only considered the weak-charge form factors at the relevant momentum transfers of CREX and PREX-II, namely, $q_{\rm CREX} = 0.778$ fm^{-1} and $q_{\rm PREX} = 0.475$ fm^{-1}. We now explore the sensitivity of the correlation between the neutron radius and the weak-charge form factor as a function of the momentum transfer q. This is particularly relevant because the optimal momentum transfer emerges from a compromise between the elastic cross section, which falls rapidly with q, and the parity-violating asymmetry, which is proportional to q^2. However, it is *a priori* unclear whether at an optimal momentum transfer (which is not small) the correlation between the weak-charge form factor and the neutron radius is strong.

We begin by displaying in Fig. 3 the weak-charge form factors for both ^{48}Ca and ^{208}Pb with their associated theoretical uncertainties as a function of q. Note that in order to make the theoretical errors visible they had to be amplified by a factor of 10. The results show clearly the faster falloff of $F_W^{208}(q)$ due to its larger weak-charge radius. In particular, this allows CREX to go to a higher momentum transfer where the parity-violating asymmetry is larger. At the values of the proposed momentum transfers, the predicted form factors are almost equal, i.e., $F_W^{48} \approx F_W^{208} \approx 0.2$. Note that the predictions from the nonrelativistic SV-min and the relativistic FSUGold agree very well with each other and both are consistent with the PREX measurement. We emphasize that, although some model-dependent assumptions must be invoked in extracting the neutron radius from a measurement of the form factor, such assumptions are ultimately unnecessary. This is because one can always compare the theoretical form factors directly with experiment.

We now explore the correlation between r_n^{208} and $F_W^{208}(q)$ for a range of momentum transfer. In Fig. 4(a) we compare

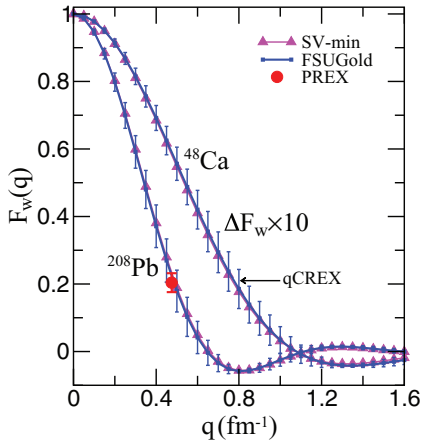

FIG. 3. (Color online) Weak-charge form factors with corresponding theoretical errors for ^{48}Ca and ^{208}Pb as predicted by SV-min and FSUGold. Note that the theoretical error bars have been artificially increased by a factor of 10. Indicated in the figure are the values of the momentum transfer appropriate for PREX-II ($q = 0.475$ fm^{-1}) and CREX ($q = 0.778$ fm^{-1}).

the (absolute value) of the correlation as predicted by SV-min and FSUGold. At small momentum transfer, the form factor behaves as $F_W(q) \approx 1 - q^2 r_W^2/6 \approx 1 - q^2 r_n^2/6$ so the correlation coefficient is nearly 1. Note that we have used the fact that the weak-charge radius r_W is approximately equal to r_n [4]. Also note that, although at the momentum transfer of the PREX experiment the low-q expression is not valid, the strong correlation is still maintained. Indeed, the robust correlation is

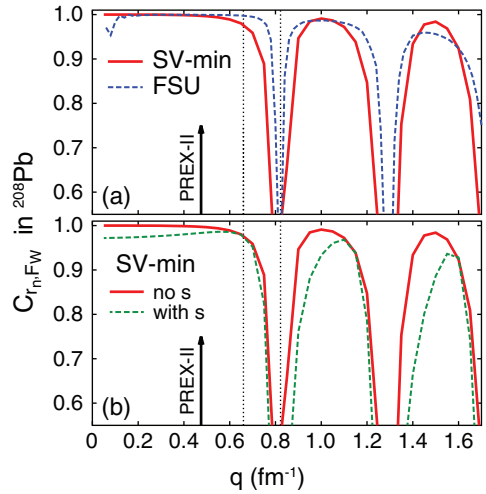

FIG. 4. (Color online) Correlation coefficient (9) between r_n^{208} and $F_W^{208}(q)$ as a function of the momentum transfer q. Panel (a) shows the absolute value of the correlation coefficient predicted by SV-min and FSUGold assuming no strange-quark contribution to the nucleon form factor. Panel (b) shows the impact of including the experimental uncertainty in the strange-quark contribution to the nucleon form factor. The arrow marks the PREX-II momentum transfer of $q = 0.475$ fm^{-1}. The first dashed vertical line indicates the position of the first zero of $F_W^{208}(q)$, the second one marks the position of the first maximum of $|F_W^{208}(q)|$ (from which the surface thickness can be deduced).

maintained at all q values, except for diffraction minima and maxima. Given the similar patterns predicted by SV-min and FSUGold, we suggest that the observed q dependence of the correlation with r_n represents a generic model feature.

Figure 4(b) displays the same correlation, but now we also include the experimental uncertainty on the strange-quark form factor. Although the strange-quark contribution to the electric form factor of the nucleon appears to be very small [47], there is an experimental error attached to it that we want to explore. For simplicity, only results using SV-min are shown with and without incorporating the experimental uncertainty on the s quark. We note that an almost perfect correlation at low-to-moderate momentum transfer gets diluted by about 6% as the uncertainty in the strange-quark contribution is included. Most interestingly, the difference almost disappears near the actual PREX point, lending confidence that the experimental conditions are ideal for the extraction of r_n^{208}. Finally, given that the strong correlation between the neutron radius and the form factor is maintained up to the first diffraction minima (about $q = 1.2$ fm^{-1} in the case of ^{48}Ca), the CREX experimental point lies safely within this range (figure not shown).

IV. CONCLUSIONS AND OUTLOOK

In this survey, we have studied the potential impact of the proposed PREX-II and CREX measurements on constraining the isovector sector of the nuclear EDF. In particular, we explored correlations between the weak-charge form factor of both ^{48}Ca and ^{208}Pb, and a variety of observables sensitive to the symmetry energy. We wish to emphasize that we have chosen the weak-charge form factor rather than other derived quantities—such as the weak-charge (or neutron) radius—since F_W is directly accessed by experiment. To assess correlations among observables, two different approaches have been implemented. In both cases we relied exclusively on models that were accurately calibrated to a variety of ground-state data on finite nuclei. In the "trend analysis," the parameters of the optimal model were adjusted in order to systematically change the symmetry energy, and the resulting impact on nuclear observables was monitored. In the "covariance analysis," we obtained correlation coefficients by relying exclusively on the covariance (or error) matrix that was obtained in the process of model optimization. From such combined analysis we find the following:

(i) We verified that the neutron skin of ^{208}Pb provides a fundamental link to the equation of state of neutron-rich matter. The landmark PREX experiment achieved a very small systematic error on r_n^{208} that suggests that reaching the total error of ± 0.06 fm anticipated in PREX-II is realistic.

(ii) We also concluded that an accurate determination of $r_{\rm skin}^{208}$ is insufficient to constrain the neutron skin of ^{48}Ca. Indeed, because of the significant difference in the surface-to-volume ratio of these two nuclei, there is a considerable spread in the predictions of the models [17]. Given that CREX intends to measure $r_{\rm skin}^{48}$ with an unprecedented error of ± 0.02 fm, this model dependence can be tested experimentally [18].

In addition, as discussed in Sec. I, there are several advantages for nuclear theory in measuring the neutron radius of both ^{48}Ca and ^{208}Pb.

(iii) We have verified that at the momentum transfer selected for PREX-II (0.475 fm^{-1}) there is a large sensitivity of the weak-charge form factor to the neutron radius of ^{208}Pb; a similar conclusion was obtained in the case of CREX.

(iv) Finally, we estimated the contribution from the strange-quark uncertainty on the electric form factor error budget. We concluded that this contribution is very small near the actual PREX q value.

In summary, although PREX-II provides a powerful constraint on the slope of the symmetry energy L, the neutron radius of ^{48}Ca is sensitive to nuclear dynamics that goes well beyond L. Thus, CREX in combination with PREX-II will constrain different aspects of the nuclear EDF. Moreover, we have reconfirmed that the electric-dipole polarizability in ^{208}Pb represents a strong isovector indicator. Hence, we strongly advocate measurements of the neutron radius and electric-dipole polarizability in ^{48}Ca. Together, these four observables—neutron radii and dipole polarizabilities in both ^{48}Ca and ^{208}Pb—will form a critical set of isovector indicators that will provide essential constraints on nuclear density functionals of the next generation.

ACKNOWLEDGMENTS

Useful discussions with the CREX Collaboration are gratefully acknowledged. This work was supported by the US Department of Energy (DOE) under Contracts No. DE-FG05-92ER40750 (FSU) and No. DE-FG02-96ER40963 (UTK), and by the BMBF under Contract No. 06ER9063.

APPENDIX: THE WEAK-CHARGE FORM FACTOR

Here, we briefly summarize the computation of the weak-charge form factor as detailed in Ref. [4]. The basic input are the local proton and neutron density distributions, ρ_p and ρ_n, respectively. Accounting for magnetic contributions would require also the spin-orbit current (for SHF) or the tensor current (for RMF) [48]. We ignore these as they add only a small correction, which is not important for this survey. The proton and neutron densities are normalized in the usual way: $\int d^3r\rho_p = Z$ and $\int d^3r\rho_n = N$. Note that Ref. [4] uses the invariant four-momentum Q^2 and the spatial momentum q side by side. They are related by $q = \sqrt{Q^2}$. We use only q throughout.

We assume spherically symmetric systems, i.e., $\rho(\mathbf{r}) = \rho(r)$ where $r = |\mathbf{r}|$. In general, $F(q)$ and $\rho(r)$ are connected through the Fourier transformation [49]

$$F(q) = \int d^3r\, e^{i\mathrm{q}\cdot\mathrm{r}}\rho(r) = 4\pi\int_0^\infty dr\, r^2\, j_0(qr)\rho(r), \quad \text{(A1a)}$$

$$\rho(r) = \int \frac{d^3q}{8\pi^3}\, e^{-i\mathrm{q}\cdot\mathrm{r}}F(q) = \frac{1}{2\pi^2}\int_0^\infty dq\, q^2\, j_0(qr)F(q). \quad \text{(A1b)}$$

The transformation applies to any local density, for protons $\rho_p \longleftrightarrow F_p$, neutrons $\rho_n \longleftrightarrow F_n$, and the weak-charge density $\rho_W \longleftrightarrow F_W$.

We prefer to formulate the weak-charge distributions in terms of the form factor because the necessary folding operations become much simpler in the Fourier space. The weak charge form factor normalized to one at $q = 0$ can be written as

$$F_W(q) = e^{a_{\mathrm{cm}}q^2}\frac{G_n^Z(q)F_n(q) + G_p^Z(q)F_p(q)}{G_n^Z(0)F_n(0) + G_p^Z(0)F_p(0)}, \quad \text{(A2)}$$

with

$$G_p^Z = \mathcal{N}_p\left[\frac{G_p - G_n}{4} - S_{\Theta_W}G_p - \frac{G_s}{4}\right], \quad \text{(A3a)}$$

$$G_n^Z = \mathcal{N}_n\left[\frac{G_n - G_p}{4} - S_{\Theta_W}G_n - \frac{G_s}{4}\right], \quad \text{(A3b)}$$

$$G_s(q) = \rho_s\frac{\hbar^2q^2/(4c^2M^2)}{1 + 4.97\hbar^2q^2/(4c^2M^2)}, \quad \text{(A3c)}$$

$$\mathcal{N}_p = \frac{0.0721}{1 - 4\sin^2(\Theta_W)}, \quad \mathcal{N}_n = 0.9878, \quad \text{(A3d)}$$

where G_p and G_n are the standard proton and neutron electromagnetic form factors, respectively; G_s is the strange-quark electric form factor; $S_{\Theta_W} = \sin^2(\Theta_W) = 0.23$; $\rho_s = (-0.24 \pm 0.70)$ fm; M is the average nucleon mass; and a_{cm} a parameter for the center-of-mass (c.m.) correction. The renormalization factors $\mathcal{N}_p$, $\mathcal{N}_n$ take into account the radiative corrections to the weak charge [50]. They guarantee that the weak-charge becomes 0.0721 for the proton and -0.9878 for the neutron. The simple renormalization by a constant factor assumes that the corrections do not change significantly over the range of q relevant for the PREX measurements.

The strength ρ_s of the s-quark coupling and its uncertainties are taken from Refs. [47,51]. These two evaluations agree in the strength and have slightly different values for the uncertainties. In this work, we took the average of both.

A word is in order about the c.m. correction. The variance of the c.m. momentum $\langle\hat{P}^2_{\mathrm{c.m.}}\rangle$ is computed in SCMF models from the actual wave function to define the coefficient

$$a_{\mathrm{c.m.}} = \frac{\hbar^2}{8\langle\hat{P}^2_{\mathrm{c.m.}}\rangle}. \quad \text{(A4a)}$$

One often uses a simple estimate for the c.m. correction energy from a harmonic oscillator shell model. In this context, it is consistent to make the replacement

$$a_{\mathrm{c.m.}} = \frac{1.58}{6.0A^{2/3}}\ \mathrm{fm}^2, \quad \text{(A4b)}$$

where A is the mass number.

TABLE I. Parameters of the model (A5) for the nucleon form factors. The constants b_i are given in units fm^{-2}. E_0 is the isoscalar ($I = 0$) electric form factor and E_1 the isovector one ($I = 1$). The form factors are taken from [52].

	a_1	a_2	a_3	a_4	b_1	b_2	b_3	b_4
E_0	2.2907	−0.6777	−0.7923	0.1793	15.75	26.68	41.04	134.2
E_1	0.3681	1.2263	−0.6316	0.0372	5.00	15.02	44.08	154.2

The weak-charge form factor is expressed in terms of the intrinsic nucleon form factors. We use here the traditional form of Simon and Walther [52,53]. It parametrizes isoscalar and isovector form factors as a sum of dipole terms:

$$G^{(\mathrm{S})}_{\mathrm{typ}}(q) = \sum_{\nu=1}^{4} \frac{a_{\mathrm{typ},\nu}}{1 + q^2/b_{\mathrm{typ},\nu}} \tag{A5}$$

with $\mathrm{typ} \in \{\text{“}E, I = 0\text{”}, \text{“}E, I = 1\text{”}\}$ and with parameters listed in Table I. The proton and neutron Sachs form factors are

$$G^{(\mathrm{S})}_{E,p} = \tfrac{1}{2}\left(G^{(\mathrm{S})}_{E,I=0} + G^{(\mathrm{S})}_{E,I=1}\right), \tag{A6a}$$

$$G^{(\mathrm{S})}_{E,n} = \tfrac{1}{2}\left(G^{(\mathrm{S})}_{E,I=0} - G^{(\mathrm{S})}_{E,I=1}\right). \tag{A6b}$$

[1] S. Abrahamyan *et al.*, Phys. Rev. Lett. **108**, 112502 (2012).
[2] C. J. Horowitz *et al.*, Phys. Rev. C **85**, 032501 (2012).
[3] T. Donnelly, J. Dubach, and I. Sick, Nucl. Phys. A **503**, 589 (1989).
[4] C. J. Horowitz, S. J. Pollock, P. A. Souder, and R. Michaels, Phys. Rev. C **63**, 025501 (2001).
[5] X. Roca-Maza, M. Centelles, X. Viñas, and M. Warda, Phys. Rev. Lett. **106**, 252501 (2011).
[6] K. Paschke *et al.*, PREX-II Proposal to Jefferson Lab, 2012, http://hallaweb.jlab.org/parity/prex/prexII.pdf
[7] J. D. Holt, T. Otsuka, A. Schwenk, and T. Suzuki, J. Phys. G **39**, 085111 (2012).
[8] G. Hagen, M. Hjorth-Jensen, G. R. Jansen, R. Machleidt, and T. Papenbrock, Phys. Rev. Lett. **109**, 032502 (2012).
[9] S. Riordan *et al.*, CREX Proposal to Jefferson Lab, 2013, http://hallaweb.jlab.org/parity/prex/c-rex2013_v7.pdf
[10] J. Erler, N. Birge, M. Kortelainen, W. Nazarewicz, E. Olsen, A. Perhac, and M. Stoitsov, Nature (London) **486**, 509 (2012).
[11] J. Erler, C. J. Horowitz, W. Nazarewicz, M. Rafalski, and P.-G. Reinhard, Phys. Rev. C **87**, 044320 (2013).
[12] A. Ekström, G. Baardsen, C. Forssén, G. Hagen, M. Hjorth-Jensen, G. R. Jansen, R. Machleidt, W. Nazarewicz, T. Papenbrock, J. Sarich, and S. M. Wild, Phys. Rev. Lett. **110**, 192502 (2013).
[13] F. Wienholtz *et al.*, Nature (London) **498**, 346 (2013).
[14] A. W. Steiner and S. Gandolfi, Phys. Rev. Lett. **108**, 081102 (2012).
[15] I. Tews, T. Krüger, K. Hebeler, and A. Schwenk, Phys. Rev. Lett. **110**, 032504 (2013).
[16] K. Hebeler and R. J. Furnstahl, Phys. Rev. C **87**, 031302 (2013).
[17] J. Piekarewicz, B. K. Agrawal, G. Colò, W. Nazarewicz, N. Paar, P.-G. Reinhard, X. Roca-Maza, and D. Vretenar, Phys. Rev. C **85**, 041302 (2012).
[18] M. Kortelainen, J. Erler, W. Nazarewicz, N. Birge, Y. Gao, and E. Olsen, Phys. Rev. C **88**, 031305 (2013).
[19] M. Bender, P.-H. Heenen, and P.-G. Reinhard, Rev. Mod. Phys. **75**, 121 (2003).
[20] D. Vretenar, A. Afanasjev, G. Lalazissis, and P. Ring, Phys. Rep. **409**, 101 (2005).
[21] P.-G. Reinhard and W. Nazarewicz, Phys. Rev. C **81**, 051303 (2010).
[22] P. Klüpfel, P.-G. Reinhard, T. J. Bürvenich, and J. A. Maruhn, Phys. Rev. C **79**, 034310 (2009).
[23] M. Kortelainen, T. Lesinski, J. Moré, W. Nazarewicz, J. Sarich, N. Schunck, M. V. Stoitsov, and S. Wild, Phys. Rev. C **82**, 024313 (2010); M. Kortelainen, J. McDonnell, W. Nazarewicz, P.-G. Reinhard, J. Sarich, N. Schunck, M. V. Stoitsov, and S. M. Wild, *ibid.* **85**, 024304 (2012).
[24] F. J. Fattoyev and J. Piekarewicz, Phys. Rev. C **84**, 064302 (2011).
[25] Y. Gao, J. Dobaczewski, M. Kortelainen, J. Toivanen, and D. Tarpanov, Phys. Rev. C **87**, 034324 (2013).
[26] W. Nazarewicz, P.-G. Reinhard, W. Satuła, and D. Vretenar, arXiv:1307.5782 [Eur. Phys. J. A (to be published)].
[27] P. Klüpfel, J. Erler, P.-G. Reinhard, and J. A. Maruhn, Eur. Phys. J A **37**, 343 (2008).
[28] B. D. Serot and J. D. Walecka, in *Advances in Nuclear Physics*, edited by J. W. Negele and E. W. Vogt, Vol. 16 (Plenum Press, New York, 1986), p. 1.
[29] J. Boguta and A. R. Bodmer, Nucl. Phys. A **292**, 413 (1977).
[30] P.-G. Reinhard, M. Rufa, J. Maruhn, W. Greiner, and J. Friedrich, Z. Phys. A **323**, 13 (1986).
[31] G. A. Lalazissis, J. Konig, and P. Ring, Phys. Rev. C **55**, 540 (1997).
[32] P.-G. Reinhard, Rep. Prog. Phys. **52**, 439 (1989).
[33] P. Ring, Prog. Part. Nucl. Phys. **37**, 193 (1996).
[34] J. Piekarewicz, Phys. Rev. C **69**, 041301 (2004).
[35] B. G. Todd-Rutel and J. Piekarewicz, Phys. Rev. Lett. **95**, 122501 (2005).
[36] C. J. Horowitz and J. Piekarewicz, Phys. Rev. Lett. **86**, 5647 (2001).
[37] C. J. Horowitz and J. Piekarewicz, Phys. Rev. C **64**, 062802 (2001).
[38] T. Nikšić, D. Vretenar, P. Finelli, and P. Ring, Phys. Rev. C **66**, 024306 (2002).
[39] T. Bürvenich, D. G. Madland, J. A. Maruhn, and P. G. Reinhard, Phys. Rev. C **65**, 044308 (2002).
[40] S. Brandt, *Statistical and Computational Methods in Data Analysis* (Springer, New York, 1997).
[41] A. Tamii *et al.*, Phys. Rev. Lett. **107**, 062502 (2011).
[42] R. J. Furnstahl, Nucl. Phys. A **706**, 85 (2002).
[43] P.-G. Reinhard and W. Nazarewicz, Phys. Rev. C **87**, 014324 (2013).
[44] X. Roca-Maza, M. Brenna, G. Colò, M. Centelles, X. Viñas, B. K. Agrawal, N. Paar, D. Vretenar, and J. Piekarewicz, Phys. Rev. C **88**, 024316 (2013).

[45] I. Angeli and K. P. Marinova, At. Data Nucl. Data Tables **99**, 69 (2013).
[46] J. Birkhan *et al*., RCNP experiment under analysis (unpublished).
[47] J. Liu, R. D. McKeown, and M. J. Ramsey-Musolf, Phys. Rev. C **76**, 025202 (2007).
[48] C. J. Horowitz and J. Piekarewicz, Phys. Rev. C **86**, 045503 (2012).
[49] J. Friedrich and N. Voegler, Nucl. Phys. A **373**, 192 (1982).
[50] J. Beringer *et al*. (Particle Data Group), Phys. Rev. D **86**, 010001 (2012).
[51] A. Acha *et al*. (HAPPEX Collaboration), Phys. Rev. Lett. **98**, 032301 (2007).
[52] V. H. Walther (private communication).
[53] G. G. Simon, C. Schmitt, F. Borkowski, and V. H. Walther, Nucl. Phys. A **333**, 381 (1980).